https://doi.org/10.1016/j.apenergy.2018.06.039

A feasible way to handle the heat management of direct carbon solid oxide fuel cells

Haoran Xu[1], Bin Chen[1], Peng Tan[1], Weizi Cai[1], Yiyang Wu[1], Houcheng Zhang[1,2,*], Meng Ni[1,*]

[1] *Department of Building and Real Estate, The Hong Kong Polytechnic University, Hung Hom, Kowloon, Hong Kong, China*

[2] *Department of Microelectronic Science and Engineering, Ningbo University, Ningbo 315211, China*

Abstract: A novel integrated system consisting of an external heat source, a direct carbon solid oxide fuel cell (DC-SOFC), a vacuum thermionic generator (VTIG) and a regenerator is proposed to handle the heat management of the DC-SOFC. The electrochemical/chemical reactions, ionic/electronic charge transport, mass/momentum transport and heat transfer are fully considered in the 2D tubular DC-SOFC model, which shows that the overall heat released in the cell is always different from the heat required by the internal Boudouard reaction. Three different operation strategies of the proposed system are presented, and accordingly, analytical expressions for the overall power output and efficiency for the proposed system are specified. The results show that the VTIG could effectively recover the waste heat for additional power production at a large operating current density, and the maximum power density and efficiency of the proposed system could reach more than 8100 W m^{-2} and 60% at 30000 A m^{-2} and 1173 K, respectively. The effects of the operating current density, the operating temperature and the distance between the carbon layer and anode of the DC-SOFC, and the size, anode temperature and work function of the VTIG on the performance of the proposed system are discussed through comprehensive parametric studies.

Keywords: Solid oxide fuel cell; Carbon gasification; Vacuum thermionic generator; Heat management; Performance improvement

*Corresponding authors.

Email addresses: zhanghoucheng@nbu.edu.cn (H. Zhang), bsmengni@polyu.edu.hk (M. Ni).

1. Introduction

Despite the tendency in decreasing the reliance on fossil fuels and the development of alternative renewable energy technologies due to energy crisis and relative environmental problems, solid carbon remains a main resource in the coming decades because of its abundant storage and low price [1]. However, the utilization of solid carbon in conventional thermal plants for electricity generation is low-efficient due to the limitation Carnot cycle and complex intermediate processes [2]. In addition, the pollution from thermal plants cause various environmental problems, *e.g.* acid rains and global warming. Therefore, an alternative high-efficient and clean energy conversion device for electricity generation from solid carbon is urgently needed, such as solid oxide fuel cells (SOFCs) [3, 4].

An SOFC is a whole solid-state device with a dense electrolyte sandwiched between two porous electrodes. As one of the most attractive energy conversion devices, SOFCs can directly convert gaseous fuels, such as H_2 and CO, into electricity through electrochemical reactions. The fuel flexibility characteristic of SOFCs also allows the utilization of other fuels, such as methane and solid carbon [5, 6]. Solid carbon is an attractive fuel since it has a high volumetric energy density compared with gaseous fuels. Moreover, solid carbon is cheap and abundant, bringing huge economic advantages in exploring new markets [7-9]. However, the large particle size of solid carbon limits its direct contact with the triple phase boundaries (TPBs) in porous anode, resulting in a low output power density of direct carbon solid oxide fuel cells

(DC-SOFCs). To overcome this problem, *in situ* solid carbon gasification has been proposed. Through *in situ* gasification, solid carbon is converted to gaseous fuel (*e.g.* CO) before the electrochemical reaction, which keeps the high volumetric energy density of solid carbon and expands the electrochemical reaction area simultaneously. A number of studies have been conducted to further improve the performance of DC-SOFC by adopting catalysts for faster carbon gasification kinetics [10-13]. Moreover, it has been found that DC-SOFCs can co-generate fuel and electricity power, which further increases their economic advantage [14-18]. The thermal effect in DC-SOFC has been also studied to examine its potential for combined heat, gaseous fuel and electricity power generation [19]. It was found that the DC-SOFC requires heat input at a small current density due to the endothermic carbon gasification reaction, while the cell releases waste heat at a large operating current density. Initial studies combining conventional Stirling cycle and Otto heat engine with the DC-SOFC for its performance improvement have been conducted [20, 21]. However, a system combining DC-SOFC with more novel and advanced heat-to-electricity conversion device is still needed to examine the potential performance improvement.

A vacuum thermionic generator (VTIG) consists of an emitter (*i.e.*, cathode) and a collector (*i.e.*, anode) with a vacuum gap between them [22-24]. A VTIG can directly convert thermal energy into electricity using electron gas as working fluid based on the principle of thermionic emission [25-29]. The VTIG offers many advantages, such as being quiet, efficient, compact and environmental-friendly, but it requires a high-temperature heat source to generate an electrical current for practical usage [30, 31]. VTIGs normally operate at a high temperature

(above 1600 K) with high efficiency (above 50%) and are often used as topping cycles for power generation [32, 33]. It is difficult to operate the VTIG at a low temperature because the high work function of common metallic cathodes cannot produce sufficient electron emission at a low temperature. Recently, Liang et al. [34, 35] proposed a single-layer graphene cathode-based VTIG and found that it was possible for the cathode to emit a sufficiently high current density at 700-1000 K. Obviously, the reduced operating temperature provides an opportunity for VTIG to act as a bottoming cycle for waste heat recovery for DC-SOFCs.

The literature survey shows that no research has been reported on the heat management of the DC-SOFCs using the VTIG yet. In this work, an external heat source and a VTIG are adopted and integrated to handle the heat management problem of a DC-SOFC. The thermal characteristics of the DC-SOFC are revealed using a 2D tubular model, in which the electrochemical/chemical reactions, ion/electronic charge transport, mass/momentum transport and heat transfer are fully considered. The operation modes of the proposed system are specified under different operating conditions, and accordingly, the mathematical expressions for output power and efficiency of the proposed system are given, respectively. The feasibility and effectiveness of the proposed system are also shown through numerical calculations. Finally, the effects of several design parameters and operation conditions on the performance of the proposed system are discussed.

2. System description

As shown in Fig. 1, the proposed system mainly consists of a DC-SOFC, an external heat source, a VTIG and a regenerator. The DC-SOFC generates electricity (P_{SOFC}) by consuming inlet solid carbon. If the DC-SOFC operates at an endothermic mode, an amount of heat $|Q_{SOFC}|$ should be provided from the external heat source to ensure the normal operation of the DC-SOFC, as shown in Fig. 1 (b). If the DC-SOFC operates at an exothermic mode, excessive waste heat generated in the cell Q_{SOFC} is transferred to the VTIG for additional power generation, as shown in Fig. (c). The regenerator functions as a counter-flow heat exchanger that preheats the low-temperature inlet reactants with the help of the high-temperature outlet gases.

For simplification, the following assumptions are adopted for DC-SOFC and VTIG models [14]:

- Electrochemical reactions spatially take place at TPBs, which are assumed to be uniformly distributed in the porous electrodes;
- Electronic and ionic conduction phases in the porous electrodes are continuous and homogeneous;
- All gases involved in the DC-SOFC are ideal gases and the gas flows are incompressible;
- Difference of the temperature between the anode and the carbon is negligible;
- Heat transfer irreversibility between the DC-SOFC and the VTIG is neglected;

- Inter-electrode gap in the VTIG is small and the space charge effect is neglected;
- Areas of the two plates of VTIG are assumed to be identical.

2.1 DC-SOFC

The schematic of the electrolyte-supported tubular DC-SOFC is shown in Fig. 2 (a). Solid carbon is supplied to the anode chamber and air is supplied to the cathode channel. The solid carbon reacts with CO_2 to form CO molecules (Boudouard reaction). The produced CO molecules diffuse into the porous anode and reacts with O^{2-} at the TPB sites to form CO_2 molecules, which subsequently diffuse back to the anode chamber to maintain the Boudouard reaction. Through these self-sustained processes, electrical power can be continuously generated.

The well-developed 2D model is adopted to describe the electrochemical/chemical reactions, ionic/electronic charge transport, mass/momentum transport and heat transfer in the tubular DC-SOFC [14]. The 2D DC-SOFC model has been validated in the previously study [14] with good agreement between the simulation results and the experimental data reported in Ref. [36]. In the following, the sub-models for the 2D DC-SOFC will be briefly described.

2.2.1 Chemical reaction model

The key chemical reaction in DC-SOFC is the Boudouard reaction (Eq. (1)), which converts solid carbon into CO by consuming CO_2. The reaction rate for the Boudouard reaction can be calculated by Eq. (2).

$$\mathrm{C} + \mathrm{CO_2} = 2\mathrm{CO} \quad (1)$$

$$R_{rb} = k_{rb}\exp(-E_{rb}/RT)c_{\mathrm{CO_2}} \quad (2)$$

2.2.2 Electrochemical reaction model

In the electrochemical reaction model, CO is the fuel that directly participates in electrochemical reactions. CO molecules produced from Boudouard reaction will transport from anode chamber to electrode TPB sites where they electrochemically react with O^{2-} ions and release electrons, as shown by Eq. (3). At the cathode, the O_2 molecules in the air are reduced to O^{2-} ions (as shown by Eq. (4)), which are transported from the cathode to the anode

$$CO + O^{2-} \rightarrow CO_2 + 2e^- \quad (3)$$

$$O_2 + 4e^- \rightarrow 2O^{2-} \quad (4)$$

The related equilibrium potential (E) for the electrochemical reactions can be calculated as Eq. (5) [14]

$$E = E_{CO}^0 + \frac{RT}{2F} \ln \left[\frac{p_{CO}^L (p_{O_2}^L)^{1/2}}{p_{CO_2}^L} \right] \quad (5)$$

where R is the universal gas constant, T is the operating temperature, F is the Faraday's constant, p^L is the local gas partial pressure. E_{CO}^0 is the standard potential for CO, which can be calculated by Eq. (6) [14]

$$E_{CO}^0 = 1.46713 - 0.0004527T \quad (6)$$

As local gas partial pressure is used in the calculation, only activation overpotential loss (η_{act}) and ohmic overpotential losses (η_{ohmic}) are considered for the calculation of the output voltage (V):

$$V = E - \eta_{act} - \eta_{ohmic} \quad (7)$$

According to the Butler-Volmer equation and ohm law, the activation overpotential loss η_{act} and ohmic overpotential losses η_{ohmic} can be, respectively, calculated by [14, 15]

$$i = i_0 \left\{ \exp\left(\frac{\alpha n F \eta_{act}}{RT}\right) - \exp\left(\frac{(1-\alpha) n F \eta_{act}}{RT}\right) \right\} \quad (8)$$

and

$$i = -\sigma^{eff} \nabla(\phi) \quad (9)$$

where i is the operating current density, i_0 is the exchange current density, α is the electron transfer coefficient, n is the number of transferred electrons per electrochemical reaction, σ^{eff} is the effective conductivity and ϕ is electric potential, respectively.

2.2.3 Mass and momentum transport model

Mass and momentum transport are, respectively, calculated by the extended Fick's model (Eq. (10)) and the Navier-Stokes equation (Eq. (11)) [14, 15]

$$N_j = -\frac{1}{RT}\left(\frac{B_0 y_j p}{\mu}\frac{\partial \mathrm{p}}{\partial \mathrm{z}} - D_j^{eff}\frac{\partial (y_j \mathrm{p})}{\partial \mathrm{z}}\right) \quad (j = 1, \ldots, m) \quad (10)$$

$$\rho\frac{\partial u}{\partial t} + \rho u \nabla u = -\nabla p + \nabla[\mu\left(\nabla u + (\nabla u)^T\right) - \frac{2}{3}\mu\nabla u\Big] - \frac{\varepsilon\mu u}{k} \quad (11)$$

where N_j is the flux transport rate, B_0 is the permeability of the porous electrodes, y_j is the mole fraction of species *j*, μ is the gas viscosity, D_j^{eff} is the overall effective diffusion coefficient of species *j* considering both Knudsen diffusion and molecular diffusion, ρ is the gas density and *u* is the velocity vector.

2.2.4 Heat transfer model

The heat transfer process within the fuel cell can be calculated by the general heat balance

equation [16]:

$$\rho C_p u \cdot \nabla T + \nabla \cdot \left(-\lambda_{eff} \nabla T\right) = Q \quad (12)$$

where C_p is the constant-pressure heat capacity of fluid, λ_{eff} is the effective heat conductivity and Q is the heat source term.

The electrical efficiency of DC-SOFC is defined as:

$$\eta_{SOFC} = \frac{P_{SOFC}}{P_{SOFC} + Q_{SOFC}} \quad (13)$$

where P_{SOFC} is the electrical power output and Q_{SOFC} is the rate of heat rejection of the DC-SOFC.

The electrical power output can be calculated as the multiplication of output voltage and electrical current (I):

$$P_{SOFC} = V \times I \quad (14)$$

The heat rejection rate from DC-SOFC is a positive value at a high operating current, which is the difference between the heat generation rate (Q_e) and the heat consumption rate in Boudouard reaction (Q_b), as shown by Eq. (15)

$$Q_{SOFC} = Q_e - Q_b \quad (15)$$

where Q_e results from the thermal energy released in the electrochemical reactions and the Joule heat caused by the overpotential losses. Thus, Q_e can be further calculated as:

$$Q_e = -IT\Delta S/(2F) + (E - V)I \quad (16)$$

and Q_b equals to the enthalpy change in the Boudouard reaction.

When $Q_e = Q_b$, i.e., $Q_{SOFC} = 0$, the thermal neutral current I_{tn} for the DC-SOFC can be obtained as:

$$I_{tn} = \frac{Q_b}{-T\Delta S/(2F) + E - V_{tn}} \quad (17)$$

where V_{tn} is the thermal neutral voltage corresponding to I_{tn}.

Based on the above governing equations and the parameters in Table 1 [14, 37, 38], the curves of Q_{SOFC} and V varying with the operating current density i ($i = I/A$, A is the effective area of cell) is obtained, as shown in Fig. 2 (b). It is seen that Q_{SOFC} increases from negative to positive with the increasing i. When the heat production from electrochemical reactions is less than the heat requirement for the Boudouard reaction (i.e., $Q_{SOFC} < 0$), an amount of heat $|Q_{SOFC}|$ should be provided from the external heat source to the DC-SOFC to maintain its normal operation. In this situation, the external heat source in Fig. 1 should be connected while the VTIG is unnecessary. When $Q_{SOFC} = 0$, the DC-SOFC is thermally self-sustained and thus both the external heat source and the VTIG are unnecessary. When the heat production in the cell exceeds the heat requirement for the Boudouard reaction (i.e., $Q_{SOFC} > 0$), the VTIG should be connected to recover the excessive heat from DC-SOFC Q_{SOFC} for extra electrical power generation P_{TIG}. As also shown in Fig. 2 (b), a higher operating temperature results in a larger thermal neutral current density i_{tn} and a faster endothermic Boudouard reaction, and therefore, more heat is needed at a higher operating temperature. Therefore, less overall heat is generated for a given current density at a higher operating temperature.

2.2 Vacuum thermionic generator

When $i > i_{tn}$, the excessive heat Q_{SOFC} is flowed to the cathode of the VTIG to evaporate electrons out of the cathode surface. The escaped electrons cross the vacuum inter-electrode gap, condense at the relative cold anode, and finally return to the cathode through an external circuit [39]. The net thermionic electric current between the cathode and the anode I_{TIG} is the sum of the forward electric current from the cathode I_c and the reverse electric current from the anode I_a, and each of the electric currents can be described by the Richardson-Dushman law [22]

$$I_c = A_c A_0 T^2 \exp\left[-\Phi_c/\left(k_B T\right)\right] \tag{18}$$

and

$$I_a = A_a A_0 T_2^2 \exp\left[-\Phi_a/\left(k_B T_2\right)\right] \tag{19}$$

where A_c and A_a are, respectively, the areas of the cathode and the anode, A_0 is the Richardson-Dushmann constant, T_2 is the temperature of the anode, Φ_c and Φ_a are the work functions of the cathode and anode, respectively, $U = \left(\Phi_c - \Phi_a\right)/e$ is the output voltage of the VTIG, e is the charge of an electron, k_B is the Boltzmann constant.

Considering the radiation losses between the cathode and the anode, the rate of heat absorbed by the cathode and the rate of heat released by the anode can be, respectively, expressed as [26, 28]

$$Q_{SOFC} = \left(U + \frac{\Phi_a + 2k_B T}{e}\right) I_c - \left(U + \frac{\Phi_a + 2k_B T_2}{e}\right) I_a + A_c \varepsilon_0 \sigma \left(T^4 - T_2^4\right) \tag{20}$$

and

$$Q_2 = \frac{\Phi_a + 2k_B T}{e} I_c - \frac{\Phi_a + 2k_B T_2}{e} I_a + A_a \varepsilon_0 \sigma \left(T^4 - T_2^4 \right) \tag{21}$$

where ε_0 is the equivalent thermal emissivity of inner surfaces of cathode and anode, σ is the Stefan-Boltzmann constant. Based on Eqs. (15) and (18)-(21), one may easily numerically determine the lowest current density, i_L, from which the bottoming VTIG begins to work.

From Eqs. (18)-(21), the net thermionic electric current, power output and efficiency of the VTIG can be, respectively, expressed as

$$I_{TIG} = I_c - I_a = aAA_0 \left\{ T^2 \exp\left[-\left(\Phi_a + eU \right) / \left(k_B T \right) \right] - T_2^2 \exp\left[-\Phi_a / \left(k_B T_2 \right) \right] \right\} \tag{22}$$

$$P_{TIG} = aAA_0 U \left\{ T^2 \exp\left[-\left(\Phi_a + eU \right) / \left(k_B T \right) \right] - T_2^2 \exp\left[-\Phi_a / \left(k_B T_2 \right) \right] \right\} \tag{23}$$

and

$$\eta_{TIG} = \frac{P_{TIG}}{Q_{SOFC}} \tag{24}$$

where $a = A_c / A$ is the ratio between the electrode area of the VTIG and the electrode area of the DC-SOFC.

Based on the parameters given in Table 1 and Table 2 [26-28], one may obtain the net electric current density j_{TIG} ($j_{TIG} = I_{TIG} / A_c$) and output voltage U of the VTIG varying with the operating current density of the DC-SOFC i, as shown in Fig. 3. It is seen that i_L is larger than i_{tn}, and i_L increases as a or T_2 increases. Generally, j_{TIG} increases while U decreases with the increasing i. j_{TIG} decreases as a or T_2 increases, while U increases as a increases or T_2 decreases. The effects of a on j_{TIG} become more significant as i increases. The effects of T_2 on j_{TIG} become less sensitive as i decreases. The effects of a

on U become more significant while the effects of T_2 on U become less significant as i increases.

2.3 Regenerator

With the help of the regenerator, the products are cooled down to the environmental temperature T_0 and the solid carbon and air are heated to the operating temperature of the DC-SOFC T. According to the thermodynamic parameters provided in Ref. [40, 41], one can easily prove that the heat contained in the exhaust gas is enough to preheat the inlet reactants to attain the operating temperature of the DC-SOFC. Since some high-effectiveness regenerators have already been reported [42], it is proper to assume that the regenerator in Fig. 1 performs perfect regeneration.

2.4 Performance of the system

When $i \le i_L$, the VTIG is not involved in the power generation. Thus, the equivalent power output (P) and equivalent efficiency (η) of the proposed system can be, respectively, expressed as:

$$P = \begin{cases} = P_{SOFC} & (i \le i_L) \\ = P_{SOFC} + P_{TIG} & (i > i_L) \end{cases} \tag{27}$$

and

$$\eta = \begin{cases} = \dfrac{P_{SOFC}}{P_{SOFC} + |Q|} & (i \le i_L) \\ = \dfrac{P_{SOFC} + P_{TIG}}{P_{SOFC} + Q} & (i > i_L) \end{cases} \tag{28}$$

3. Results and discussion

Based on the above mathematical models and relevant parameters given in Tables 1 and 2, the performance characteristics of the proposed system can be analyzed. The parameters are taken as default ones unless mentioned specifically.

The equivalent power density and efficiency of the VTIG within the system are shown in Fig. 4, where $P_{TIG}^{*} = P_{TIG}/A$. P_{TIG}^{*} almost linearly increases as i increases, while η_{TIG} first quickly and then slowly increases as i increases. Both P_{TIG}^{*} and η_{TIG} increase as a or T_2 decreases. The effects of a on the performance of VTIG become less significant as i increases, while the effects of T_2 on the performance of VTIG become more significant as i increases. At given operating conditions, the performance of VTIG becomes less sensitive to T_2 as T_2 decreases, P_{TIG}^{*} and η_{TIG} slightly change when T_2 drops from 600 K to 300 K [43].

The power densities of the DC-SOFC, the VTIG and the proposed system are compared at different operating temperatures, as shown in Fig. 5, where $P_{SOFC}^{*} = P_{SOFC}/A$ and $P^{*} = P/A$ are the power densities for the DC-SOFC and the proposed system, respectively. When $i \le i_L$, the curves of $P^{*} \sim i$ and $P_{SOFC}^{*} \sim i$ are overlapped as the VTIG is not involved in power generation. When $i > i_L$, P_{TIG}^{*} keeps growing with increasing operating current density as more heat is provided to the VTIG from the DC-SOFC. Following a different trend, the power density of the DC-SOFC P_{SOFC}^{*} first increases and then decreases with the increasing i. The power density magnitude of VTIG is the same as that of the DC-SOFC. As a result, the power

density of the proposed system is obviously improved compared with the power density of the sole DC-SOFC.

For a given operating current density, the performance of the DC-SOFC is improved with increasing operating temperature as the elevated operating temperature promotes the chemical/electrochemical reactivity, ionic conductivity and gas effective diffusion. Additionally, a higher operating temperature provides a smaller slope for output voltage reduction, and consequently, the higher operating temperature extends the operating current density range of the DC-SOFC. It is seen from Fig. 5 that i_L increases as the operating temperature increases. For a given operating current density, the power density of the VTIG decreases with increasing operating temperature because less waste heat is supplied to the VTIG, as shown by Fig. 2. As the increase in P_{SOFC}^* is more significant than the decrease in P_{TIG}^*, a higher operating temperature is more preferable for the proposed system to obtain a higher overall power density P^*. For example, when the DC-SOFC operates at a current density of 30000 A m^{-2}, the power density of the proposed system P^* approximately increases from 5580 W m^{-2} at 1073 K to 8100 W m^{-2} at 1173 K, which are about 81.5% and 36.4% larger than that of the stand-alone DC-SOFC, respectively.

The efficiencies of the DC-SOFC, the VTIG and the proposed system under different operating temperature are shown in Fig. 6. Similarly, the curves of $\eta \sim i$ and $\eta_{SOFC} \sim i$ are overlapped in the region of $i \le i_L$, in which both η and η_{SOFC} first increase to 100% at i_{tn} and then decrease to a certain value at i_L. It is seen that both i_{tn} and i_L are increased as the operating temperature T increases. When $i \le i_L$, η decreases as the operating temperature

T increases. When $i > i_L$, η is always larger than η_{SOFC}. When the DC-SOFC works at a current density of 30000 A m^{-2}, the efficiency of the proposed system η increases from 47.5% at 1073 K to 61.8% at 1173 K, and the efficiency of the DC-SOFC η_{SOFC} increases from 26.4% at 1073 K to 45.4% at 1173 K. A higher operating temperature is thus more favored for the proposed system to achieve a better performance, as shown in Fig. 7.

The effects of a on the system performance are only in the region of $i > i_L$, as shown in Fig. 8. It is observed that both P^* and η are increased as a decreases. The effects of a on the system performance become less significant as the operating current density i increases. The effects of the anode temperature of VTIG (T_2) on the proposed system performance happen only in the region of $i > i_L$, as shown in Fig. 9. It is observed that the performance of the proposed system is improved as T_2 decreases, and this effect becomes less prominent as T_2 decreases from 800K to 600 K. When $i > i_L$, the effects of T_2 on the proposed system performance become more significant as the operating current density increases.

In DC-SOFCs, the distance between carbon layer and anode D_{ce} will increase accompanying the consumption of solid carbon. Thus, the gas transportation between carbon layer and anode could significantly affect the electrical power output P_{SOFC} and heat generation Q_{SOFC}. As shown in Fig. 10, both P^* and η are improved as D_{ce} decreases from 559 μm to 59 μm. At given conditions, the peak power density $P^*_{\max}$ increases from 5000 W m^{-2} at 559 μm to 7230 Wm^{-2} at 59 μm. As analyzed in our previous papers [14, 19], a small distance between carbon layer and anode helps maintain a high fuel concentration in the anode, which results in a high output power density of the DC-SOFC. It is also shown that the effects of D_{ce}

on the system performance become more pronounced at a larger current density because more heat is produced in the DC-SOFC at a higher operating current density.

Work function Φ_a is a parameter that measures the minimum energy necessary to bring an electron outside of the anode of the VTIG. Similar to other VTIG related parameters, the effects of Φ_a take place only in the region of $i > i_L$. It is seen from Fig. 11 that the performance of the proposed system is improved as the work function decreases because it is easier for the VTIG to emit electrons with a lower work function anode. The effects of Φ_a on the system performance become more significantly with the increasing operating current density i.

4. Conclusions

A new system consisting of a DC-SOFC, an external heat source, a VTIG and a regenerator is proposed to handle the heat management of the DC-SOFC. A previously developed 2D tubular DC-SOFC model shows that the overall heat generated in the cell could be smaller than, equal to or larger than the heat required by the internal Boudouard reaction. According to the thermal characteristics of the DC-SOFC, three operation modes are presented. The analytical expressions for power output and efficiency of the proposed system under different operating conditions are specified. The results show that the proposed system is technically feasible and effective, and the power density and efficiency of the proposed system could be more than 8100 W m^{-2} and 60%, respectively. Comprehensive parametric studies show that the performance of the proposed system can be improved by increasing the operating

temperature and the operating current density or decreasing the distance between carbon layer and anode electrode. Furthermore, decreasing the size, anode temperature and work function of the VTIG are also beneficial to improve the performance of the proposed system. The results obtained may provide some theoretical insights into handling the heat management of a real DC-SOFC.

Acknowledgement

This research is supported by the National Natural Science Foundation of China (Grant No. 51406091), a grant (PolyU 152127/14E) from Research Grant Council, University Grants Committee, Hong Kong SAR, and a grant from Environment and Conservation Fund (ECF 54/2015), Hong Kong SAR.

Nomenclature

Abbreviation

DC-SOFC	Direct-carbon solid oxide fuel cell
SOFC	Solid oxide fuel cell
TPB	Triple phase boundary

VTIG	vacuum thermionic generator
YSZ	Yttrium stabilized zirconium

Roman

a	Plate area ratio between VTIG and DC-SOFC
A	Effective area of DC-SOFC, m^2
A_0	Richardson-Dushmann constant,A m^{-2} K^{-2}
A_a	Area of VTIG anode, m^2
A_c	Area of VTIG cathode, m^2
B_0	Permeability coefficient, m^2
c_{CO_2}	Molar concentration of carbon dioxide, $mol \cdot m^{-3}$
C_p	Constant-pressure heat capacity,
D_i^{eff}	Effective diffusivity of species i , $m^2 \cdot s^{-1}$
e	Charge of an electron, C
E_{acv}	Activation energy, $J \cdot mol^{-1}$
E	Equilibrium potential, V
E_{CO}^0	Standard equilibrium potential for carbon monoxide oxidization, V
E_{eq}	Equilibrium Nernst potential, V
E_{rb}	Activation energy of Boudouard reaction, $J \cdot mol^{-1}$
F	Faraday constant, 96485 $C \cdot mol^{-1}$

i	Current density, $A \cdot m^{-2}$
i_L	Lowest working current density for VTIG, $A \cdot m^{-2}$
i_o	Exchange current density, $A \cdot m^{-2}$
i_{tn}	Thermal neutral current density, $A \cdot m^{-2}$
I	Electrical current, A
I_a	Reverse electric current from VTIG anode, A
I_c	Reverse electric current from VTIG cathode, A
I_{TIG}	Net thermionic electric current in VTIG, A
I_{tn}	Thermal neutral current, A
j_{TIG}	Net thermionic electric current density of VTIG, $A \cdot m^{-2}$
k_b	Boltzmann constant, $J\ K^{-1}$
k_{rb}	Kinetic coefficient of Boudouard reaction, s^{-1}
n	Number of electrons transferred per electrochemical reaction
N_i	Flux of mass transport, $kg \cdot m^{-3} \cdot s^{-1}$
p	(partial) Pressure, Pa
p_{CO}^L	Local CO gas partial pressure, Pa
$p_{CO_2}^L$	Local CO_2 gas partial pressure, Pa
$p_{O_2}^L$	Local O_2 gas partial pressure, Pa
P	Electricity power output, W
P_{SOFC}	Electricity power output by DC-SOFC, W

P_{TIG}	Electricity power output by VTIG, W
P^*	Electricity power density, W·m^{-2}
P^*_{max}	Maximum electricity power density of DC-SOFC, W·m^{-2}
P^*_{SOFC}	Electricity power density of DC-SOFC, W·m^{-2}
P^*_{TIG}	Electricity power density of VTIG, W·m^{-2}
Q	Heat, W
Q_b	Heat absorption by Boudouard reaction, W
Q_e	Heat released by electrochemical reaction, W
Q_{SOFC}	Heat rejection of DC-SOFC
R	Gas constant, 8.314 J·mol^{-1}·K^{-1}
R_{rb}	Reaction rate of Boudouard reaction, mol·m^{-3}·s^{-1}
T	Operating temperature, K
T_2	VTIG anode temperature, K
u	Velocity field, m^3·s^{-1}
U	Output voltage of VTIG, V
V	Operating voltage, V
y_i	Molar fraction of component i

Greek letters

α	Charge transfer coefficient

β_{H_2}	Electrochemical kinetics parameter for H_2
ε	Porosity
ε_0	Effective thermal emissivity
η	Electrical efficiency
η_{SOFC}	Electrical efficiency of DC-SOFC
η_{TIG}	Electrical efficiency of VTIG
η_{act}	Activation polarization, V
η_{ohmic}	Ohmic polarization, V
κ	Permeability, m^2
λ	Thermal conductivity, $W \cdot m^{-1}K^{-1}$
λ_{eff}	Effective thermal conductivity, $W \cdot m^{-1}K^{-1}$
μ	Dynamic viscosity of fluid, Pa·s
ρ	Fluid density, $kg \cdot m^{-3}$
σ	Stefan-Boltzmann constant, $W\ m^{-2}\ K^{-4}$
σ^{eff}	Effective conductivity, $S\ m^{-1}$
τ	Tortuosity
$\emptyset$	Potential, V
Φ_a	Work function of the VTIG anode, eV
Φ_c	Work function of the VTIG cathode, eV

Subscripts

an	Anode
ca	Cathode
co	Carbon monoxide
H_2	Hydrogen
l	Ionic phase
s	Electronic phase

Superscripts

0	Parameter at equilibrium conditions
eff	Effective
L	Local

References

[1] Jiang C, Ma J, Corre G, Jain SL, Irvine JTS. Challenges in developing direct carbon fuel cells. Chem Soc Rev. 2017;46:2889-912.
[2] Santini L, Accornero C, Cioncolini A. On the adoption of carbon dioxide thermodynamic cycles for nuclear power conversion: A case study applied to Mochovce 3 Nuclear Power Plant. Applied Energy. 2016;181:446-63.
[3] Mahato N, Banerjee A, Gupta A, Omar S, Balani K. Progress in material selection for solid oxide fuel cell technology: A review. Progress in Materials Science. 2015;72:141-337.
[4] Hanna J, Lee WY, Shi Y, Ghoniem AF. Fundamentals of electro- and thermochemistry in the anode of solid-oxide fuel cells with hydrocarbon and syngas fuels. Progress in Energy and Combustion Science. 2014;40:74-111.
[5] Guo Y, Bessaa M, Aguado S, Steil MC, Rembelski D, Rieu M, et al. An all porous solid oxide fuel cell (SOFC): a bridging technology between dual and single chamber SOFCs. Energy & Environmental Science. 2013;6:2119-23.
[6] Xu H, Chen B, Tan P, Cai W, He W, Farrusseng D, et al. Modeling of all porous solid oxide fuel cells. Applied Energy. 2018;219:105-13.

[7] Giddey S, Badwal SPS, Kulkarni A, Munnings C. A comprehensive review of direct carbon fuel cell technology. Progress in Energy and Combustion Science. 2012;38:360-99.
[8] Gür TM. Critical Review of Carbon Conversion in "Carbon Fuel Cells". Chemical Reviews. 2013;113:6179-206.
[9] Cao T, Huang K, Shi Y, Cai N. Recent advances in high-temperature carbon-air fuel cells. Energy & Environmental Science. 2017;10:460-90.
[10] Wu Y, Su C, Zhang C, Ran R, Shao Z. A new carbon fuel cell with high power output by integrating with in situ catalytic reverse Boudouard reaction. Electrochemistry Communications. 2009;11:1265-8.
[11] Tang Y, Liu J, Sui J. A Novel Direct Carbon Solid Oxide Fuel Cell. ECS Transactions. 2009;25:1109-14.
[12] Li C, Shi Y, Cai N. Performance improvement of direct carbon fuel cell by introducing catalytic gasification process. Journal of Power Sources. 2010;195:4660-6.
[13] Tang Y, Liu J. Effect of anode and Boudouard reaction catalysts on the performance of direct carbon solid oxide fuel cells. International Journal of Hydrogen Energy. 2010;35:11188-93.
[14] Xu H, Chen B, Liu J, Ni M. Modeling of direct carbon solid oxide fuel cell for CO and electricity cogeneration. Applied Energy. 2016;178:353-62.
[15] Xu H, Chen B, Ni M. Modeling of Direct Carbon-Assisted Solid Oxide Electrolysis Cell (SOEC) for Syngas Production at Two Different Electrodes. Journal of The Electrochemical Society. 2016;163:F3029-F35.
[16] Wu Y, Shi Y, Luo Y, Cai N. Elementary reaction modeling and experimental characterization of solid oxide direct carbon-assisted steam electrolysis cells. Solid State Ionics. 2016;295:78-89.
[17] Xu H, Chen B, Zhang H, Sun Q, Yang G, Ni M. Modeling of direct carbon solid oxide fuel cells with H2O and CO2 as gasification agents. International Journal of Hydrogen Energy. 2017;42:15641-51.
[18] Xie Y, Cai W, Xiao J, Tang Y, Liu J, Liu M. Electrochemical gas-electricity cogeneration through direct carbon solid oxide fuel cells. Journal of Power Sources. 2015;277:1-8.
[19] Xu H, Chen B, Zhang H, Kong W, Liang B, Ni M. The thermal effect in direct carbon solid oxide fuel cells. Applied Thermal Engineering. 2017;118:652-62.
[20] Xu H, Chen B, Tan P, Zhang H, Yuan J, Liu J, et al. Performance improvement of a direct carbon solid oxide fuel cell system by combining with a Stirling cycle. Energy. 2017.
[21] Xu H, Chen B, Tan P, Zhang H, Yuan J, Irvine JTS, et al. Performance improvement of a direct carbon solid oxide fuel cell through integrating an Otto heat engine. Energy Conversion and Management. 2018;165:761-70.
[22] Post AD, King BV, Kisi EH. Computational model and optimisation of a vacuum diode thermionic generator for application in concentrating solar thermal power. Applied Thermal Engineering. 2017;117:245-53.

[23] Liang SJ, Liu B, Hu W, Zhou K, Ang LK. Thermionic Energy Conversion Based on Graphene van der Waals Heterostructures. Sci Rep. 2017;7:46211.
[24] McEnaney K, Weinstein L, Kraemer D, Ghasemi H, Chen G. Aerogel-based solar thermal receivers. Nano Energy. 2017;40:180-6.
[25] Chen L, Ding Z, Zhou J, Wang W, Sun F. Thermodynamic performance optimization for an irreversible vacuum thermionic generator. The European Physical Journal Plus. 2017;132:293.
[26] Wang Y, Su S, Lin B, Chen J. Parametric design criteria of an irreversible vacuum thermionic generator. Journal of Applied Physics. 2013;114:053502.
[27] Wang Y, Su S, Liu T, Su G, Chen J. Performance evaluation and parametric optimum design of an updated thermionic-thermoelectric generator hybrid system. Energy. 2015;90:1575-83.
[28] Wang Y, Cai L, Liu T, Wang J, Chen J. An efficient strategy exploiting the waste heat in a solid oxide fuel cell system. Energy. 2015;93:900-7.
[29] Zebarjadi M. Solid-State Thermionic Power Generators: An Analytical Analysis in the Nonlinear Regime. Physical Review Applied. 2017;8.
[30] Xiao G, Zheng G, Qiu M, Li Q, Li D, Ni M. Thermionic energy conversion for concentrating solar power. Applied Energy. 2017;208:1318-42.
[31] Xiao G, Zheng G, Ni D, Li Q, Qiu M, Ni M. Thermodynamic assessment of solar photon-enhanced thermionic conversion. Applied Energy. 2018;223:134-45.
[32] Ding ZM, Chen LG, Sun FR. Optimum performance analysis of a combined thermionic-thermoelectric refrigerator with external heat transfer. Journal of the Energy Institute. 2015;88:169-80.
[33] Bellucci A, Calvani P, Cappelli E, Orlando S, Sciti D, Yogev R, et al. Preliminary characterization of ST2G: Solar thermionic-thermoelectric generator for concentrating systems. AIP Conference Proceedings. 2015;1667:020007.
[34] Liang S-J, Ang LK. Electron Thermionic Emission from Graphene and a Thermionic Energy Converter. Physical Review Applied. 2015;3:014002.
[35] Ang YS, Liang S-J, Ang LK. Theoretical modeling of electron emission from graphene. MRS Bulletin. 2017;42:505-10.
[36] Cai W, Liu J, Xie Y, Xiao J, Liu M. An investigation on the kinetics of direct carbon solid oxide fuel cells. Journal of Solid State Electrochemistry. 2016;20:2207-16.
[37] Eguchi K, Setoguchi T, Inoue T, Arai H. Electrical-Properties of Ceria-Based Oxides and Their Application to Solid Oxide Fuel-Cells. Solid State Ionics. 1992;52:165-72.
[38] Luo Y, Shi Y, Li W, Cai N. Comprehensive modeling of tubular solid oxide electrolysis cell for co-electrolysis of steam and carbon dioxide. Energy. 2014;70:420-34.
[39] Lee JH, Bargatin I, Melosh NA, Howe RT. Optimal emitter-collector gap for thermionic energy converters. Applied Physics Letters. 2012;100:173904.
[40] Todd B, Young JB. Thermodynamic and transport properties of gases for use in solid oxide fuel cell modelling. Journal of Power Sources. 2002;110:186-200.

[41] Ho FH. Graphite design handbook. ; General Atomics, San Diego, CA (US); 1988. p. Medium: P; Size: 122 p. pages.
[42] Sadrameli SM. Mathematical models for the simulation of thermal regenerators: A state-of-the-art review. Renewable and Sustainable Energy Reviews. 2016;58:462-76.
[43] Xuan XC, Li D. Optimization of a combined thermionic–thermoelectric generator. Journal of Power Sources. 2003;115:167-70.

List of Tables

Table 1. Parameters used in 2D DC-SOFC model [14, 37, 38]

Parameters	Value or expression	Unit
Ionic conductivity		
GDC	$\frac{100}{T} \times 10^{(6.66071\ -\ \frac{5322.92}{T})}$	S m^{-1}
YSZ	$3.34 \times 10^4 e^{\frac{-10300}{T}}$	S m^{-1}
Electronic conductivity		
Ag	$\frac{1.59e^8}{(0.0038T - 0.1134)}$	S m^{-1}
Porosity		
Cathode	0.46	
Anode	0.46	
Electrode volume fraction		
GDC	0.21	
Ag	0.79	
S_{TPB}		
Cathode layer	2.14×10^5	m^2 m^{-3}
Anode layer	2.14×10^5	m^2 m^{-3}
Tortuosity		
Cathode	3	
Anode	3	
Exchange current density		
CO	450	A m^{-2}
O_2	400	A m^{-2}
Charge transfer coefficient		
CO	0.5	
O_2	0.5	
Equilibrium constant of Boudouard reaction (k_{rb})	6×10^{13}	s^{-1}
Activation energy of Boudouard reaction (E_{rb})	248	kJ mol^{-1}

Table 2. Parameters used in VTIG [26-28]

Parameter	Value
Charge of an electron, e (C)	1.6×10^{-19}
Boltzmann constant, k_B (J K^{-1})	1.38×10^{-23}
Stefan-Boltzmann constant, σ (W m^{-2} K^{-4})	5.67×10^{-8}
Effective thermal emissivity, ε_0	0.18
Work function of the anode, Φ_a (eV)	1.0
Temperature of the anode, T_2 (K)	600
Richardson-Dushmann constant, A_0 (A m^{-2} K^{-2})	1.2×10^{6}
Plate area ratio between VTIG and DC-SOFC, a	0.1

List of Figures

Fig. 1.

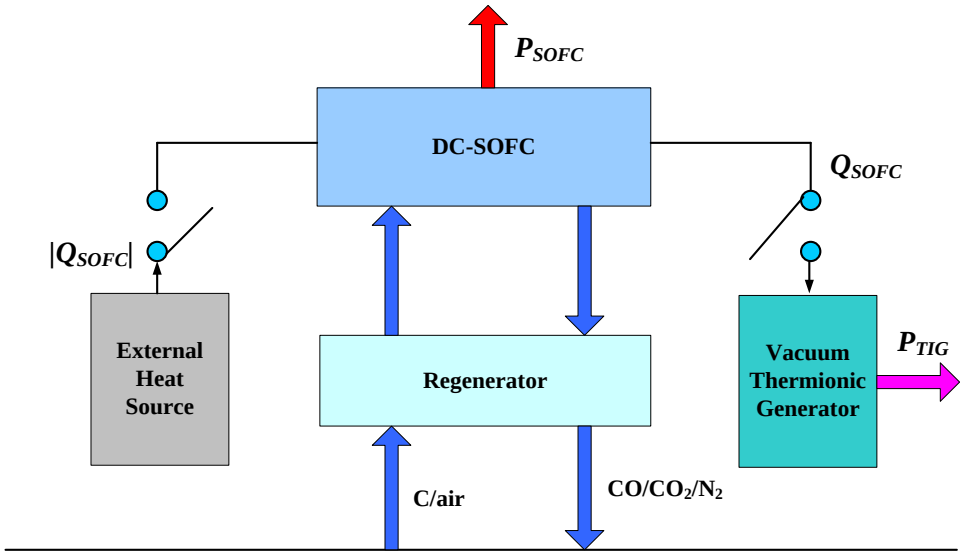
P_{SOFC}
DC-SOFC
Q_{SOFC}
$|Q_{SOFC}|$
External Heat Source
Regenerator
Vacuum Thermionic Generator
P_{TIG}
C/air
$CO/CO_2/N_2$

(a)

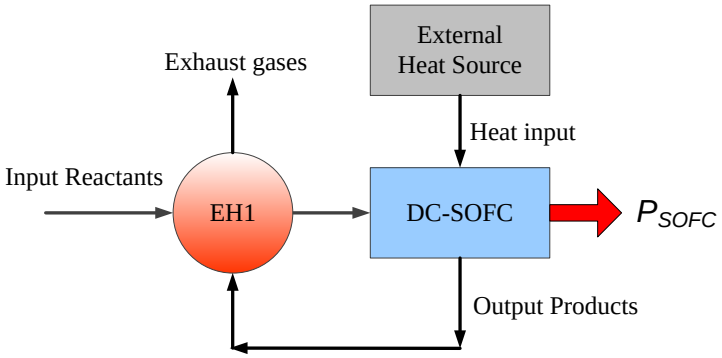
External Heat Source
Exhaust gases
Heat input
Input Reactants
EH1
DC-SOFC
P_{SOFC}
Output Products

(b)

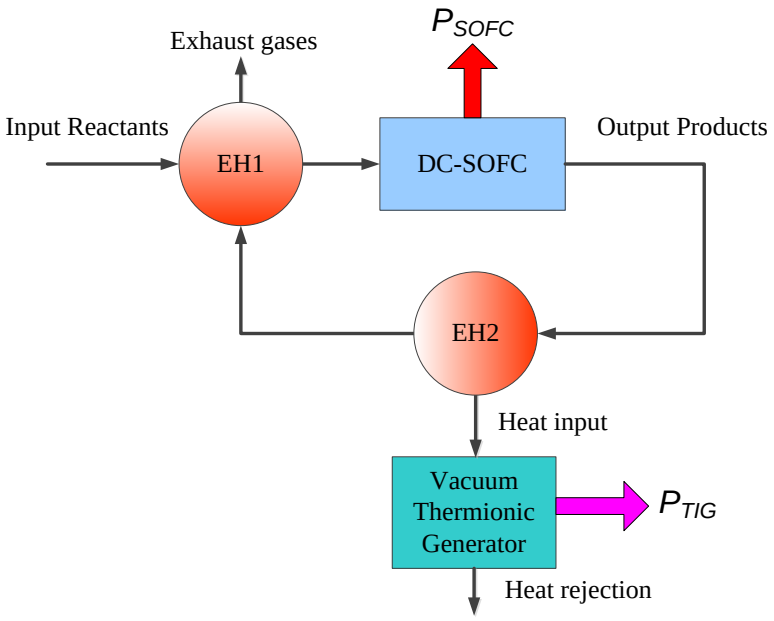

(c)

Fig. 1. (a) schematic diagram of a DC-SOFC based integrated system, (b) system layout at small operating current density, and (c) system layout at large operating current density.

Fig. 2.

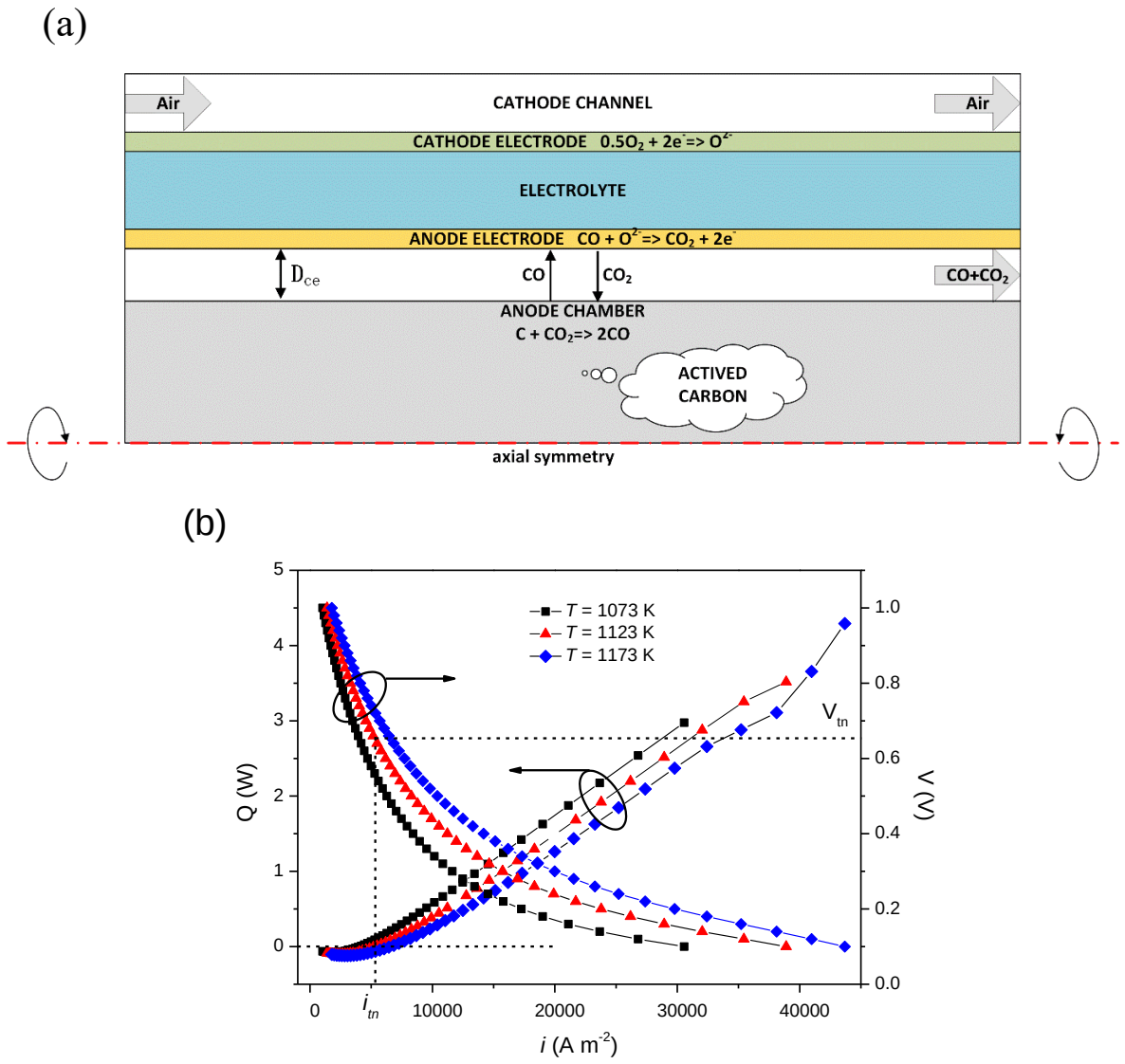

Fig. 2. (a) schematic of the 2D tubular DC-SOFC, and (b) Q_{SOFC} and V varying with the operating current density of DC-SOFC under different operating temperatures, where $i_{tn} = I_{tn}/A$ is the corresponding operating current density at I_{tn}.

Fig. 3.

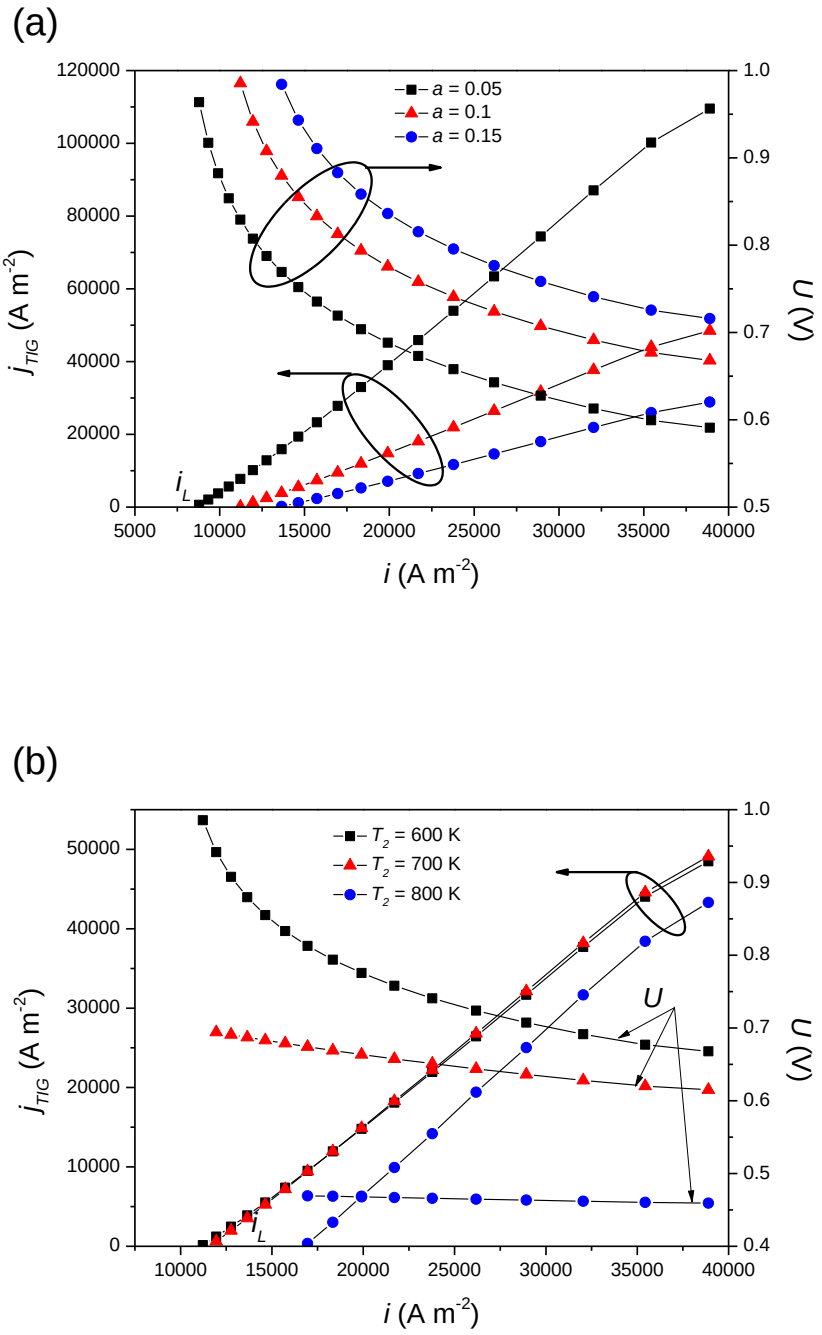

Fig. 3. Net electric current density j_{TIG} and output voltage U of the VTIG varying with the operating current density of the DC-SOFC for different (a) a, and (b) T_2.

Fig. 4.

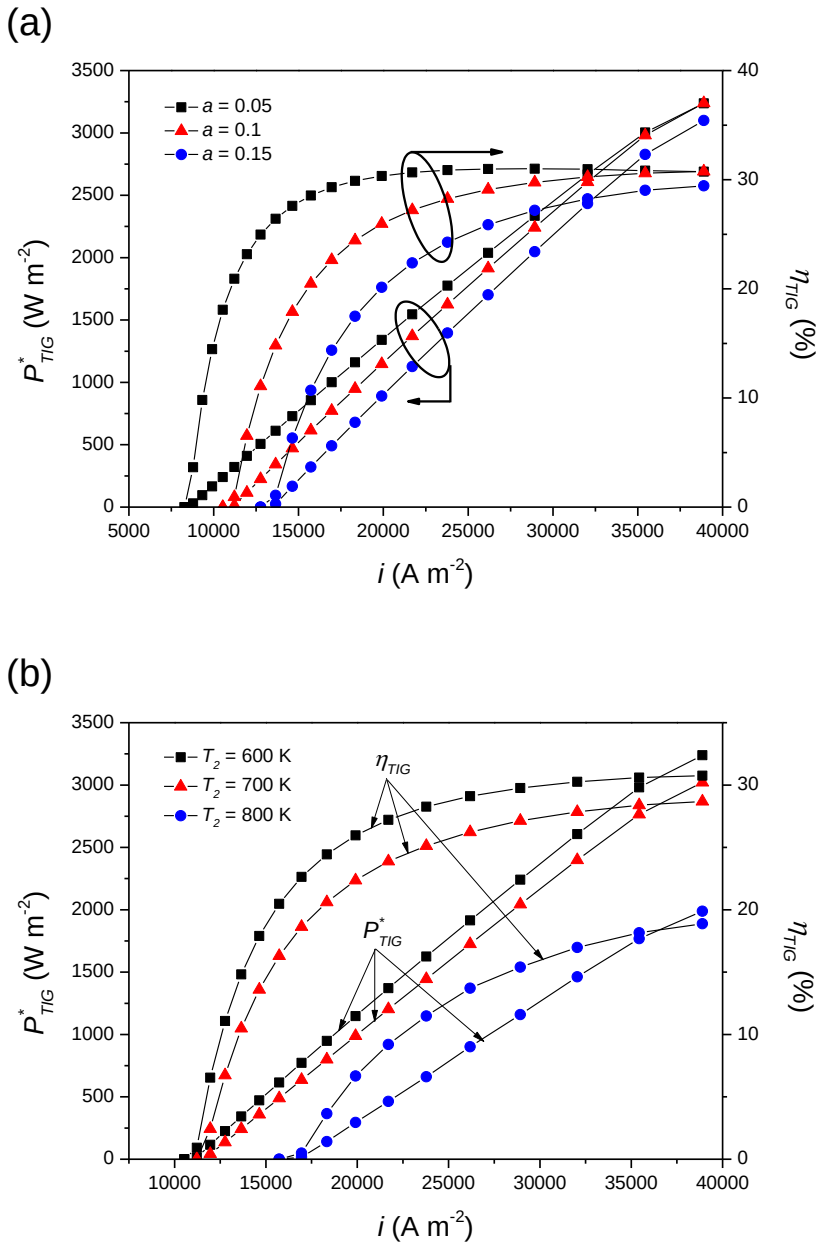

Fig. 4. Equivalent power density and efficiency of the VTIG varying with the operating current density for different (a) a, and (b) T_2.

Fig. 5.

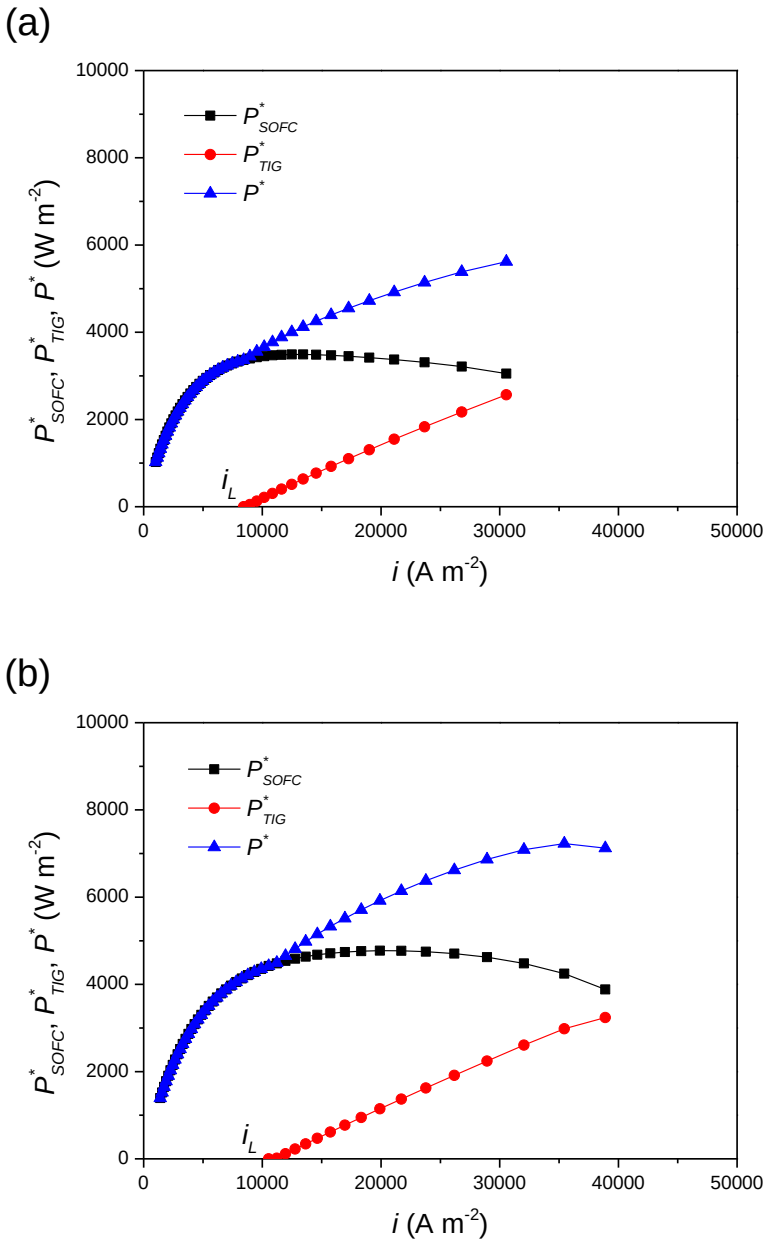
(a)
10000
8000
6000
4000
2000
0
P^*_{SOFC}
P^*_{TIG}
P^*
P^*_{SOFC}, P^*_{TIG}, P^* (W m^{-2})
i_L
0
10000
20000
30000
40000
50000
i (A m^{-2})
(b)
10000
8000
6000
4000
2000
0
P^*_{SOFC}
P^*_{TIG}
P^*
P^*_{SOFC}, P^*_{TIG}, P^* (W m^{-2})
i_L
0
10000
20000
30000
40000
50000
i (A m^{-2})

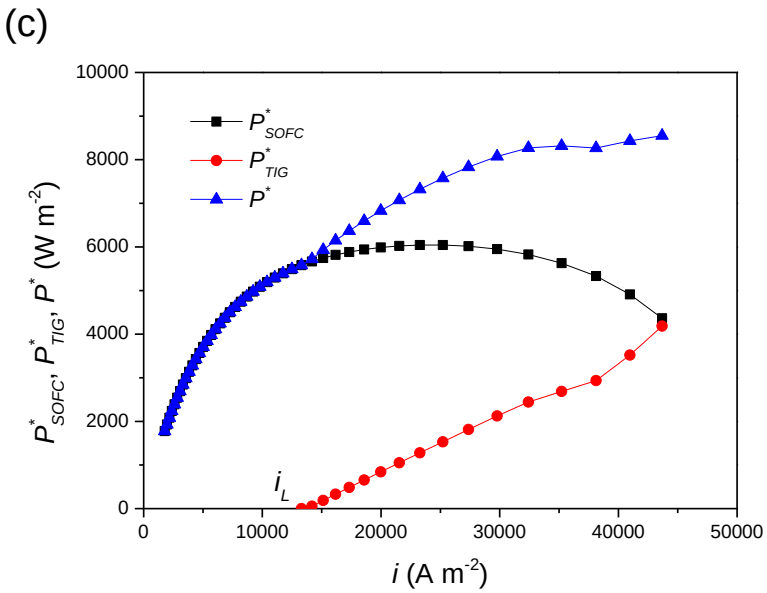

Fig. 5. Power densities of the DC-SOFC, the VTIG and the proposed system at (a) 1073 K, (b) 1123 K, and (c) 1173 K.

Fig. 6.

(a)

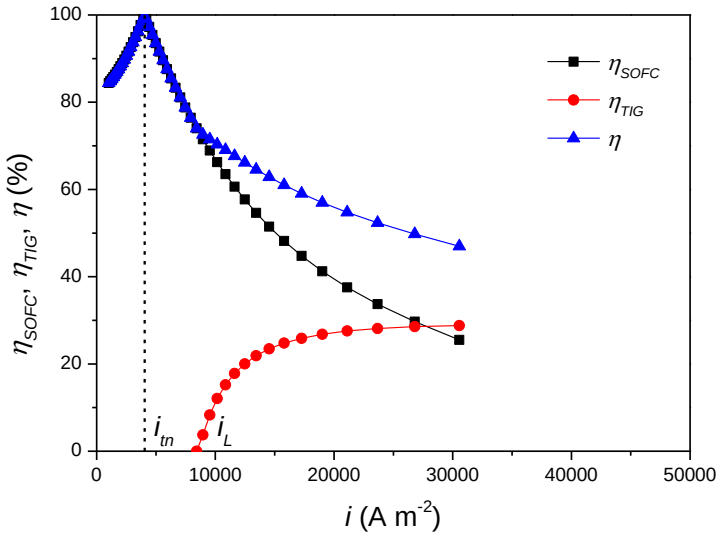
100
80
60
40
20
0
0
10000
20000
30000
40000
50000
η_{SOFC}, η_{TIG}, η (%)
i (A m^{-2})
η_{SOFC}
η_{TIG}
η
i_{tn}
i_L

(b)

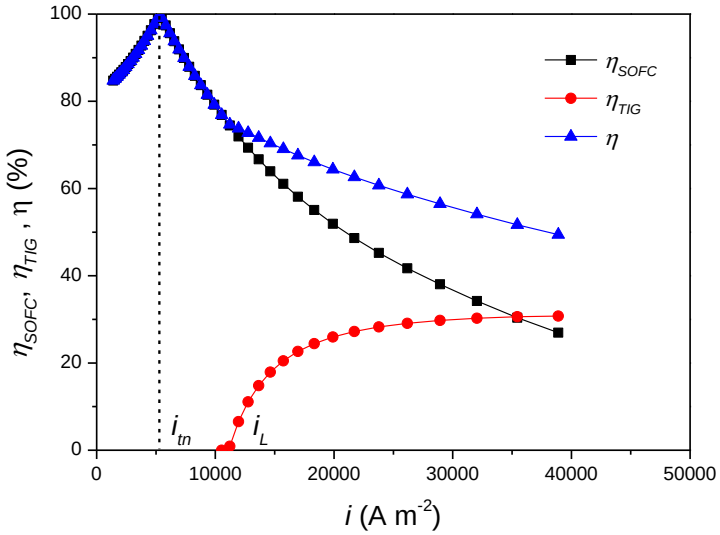
100
80
60
40
20
0
0
10000
20000
30000
40000
50000
η_{SOFC}, η_{TIG}, η (%)
i (A m^{-2})
η_{SOFC}
η_{TIG}
η
i_{tn}
i_L

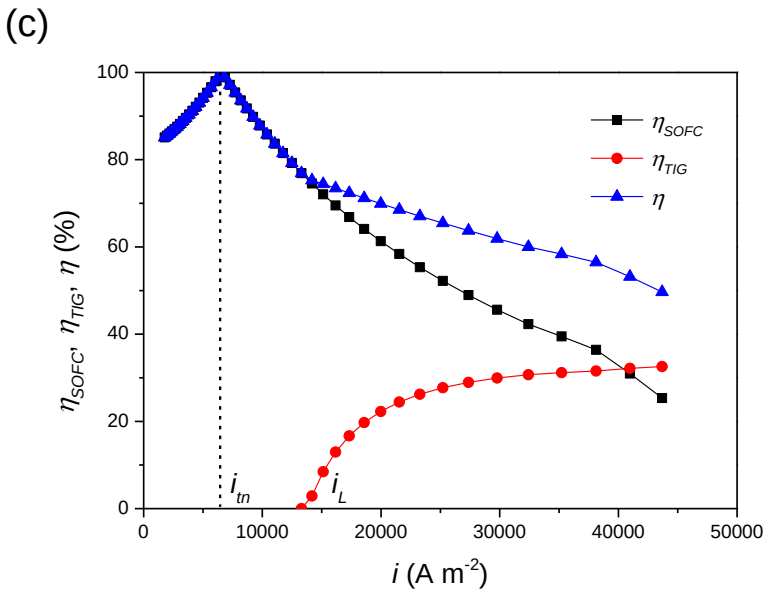

Fig. 6. Efficiencies of the DC-SOFC, the VTIG and the proposed system at (a) 1073 K, (b) 1123 K, and (c) 1173 K.

Fig. 7.

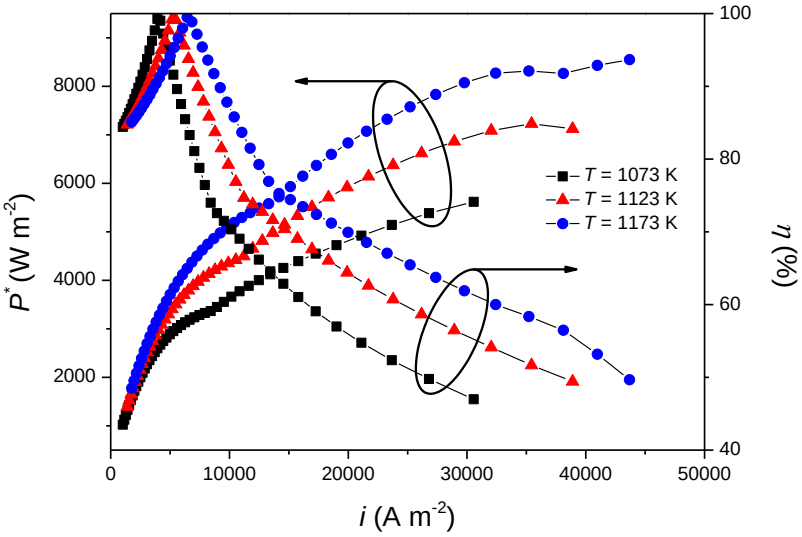

Fig. 7. Effects of the operating temperature of DC-SOFC on the system performance.

Fig. 8.

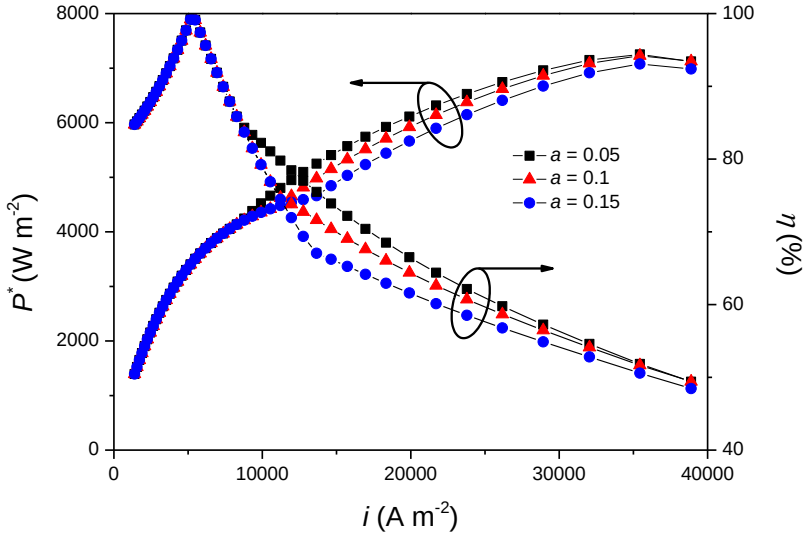

Fig. 8. Effects of the ratio between the VTIG electrode area and the DC-SOFC effective surface area on the system performance.

Fig. 9.

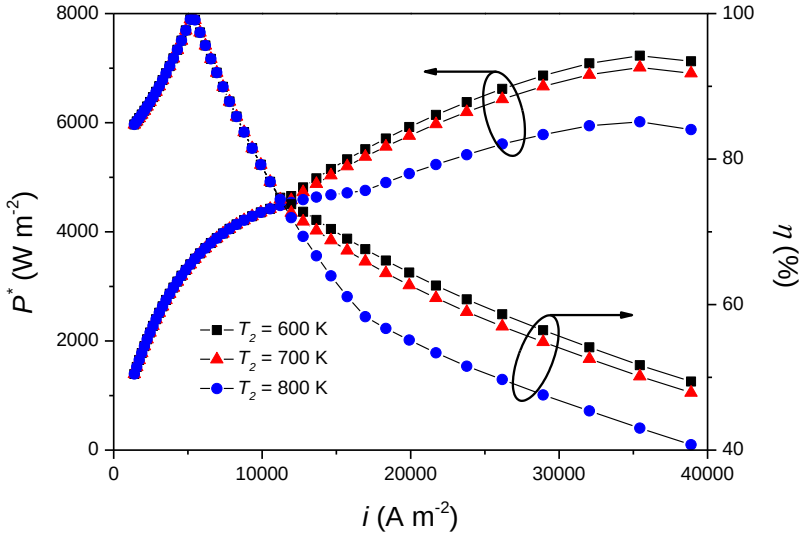

Fig. 9. Effects of the anode temperature of VTIG on the system performance.

Fig. 10.

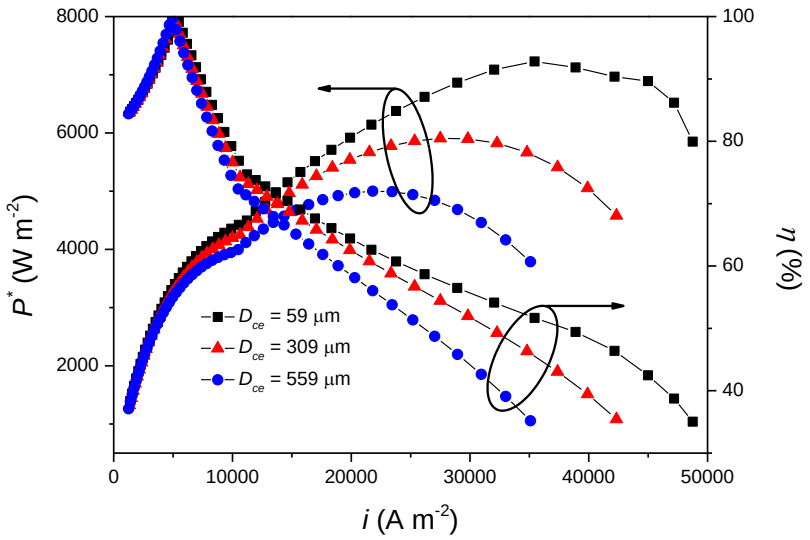

Fig. 10. Effects of the distance between carbon layer and anode on the system performance.

Fig. 11.

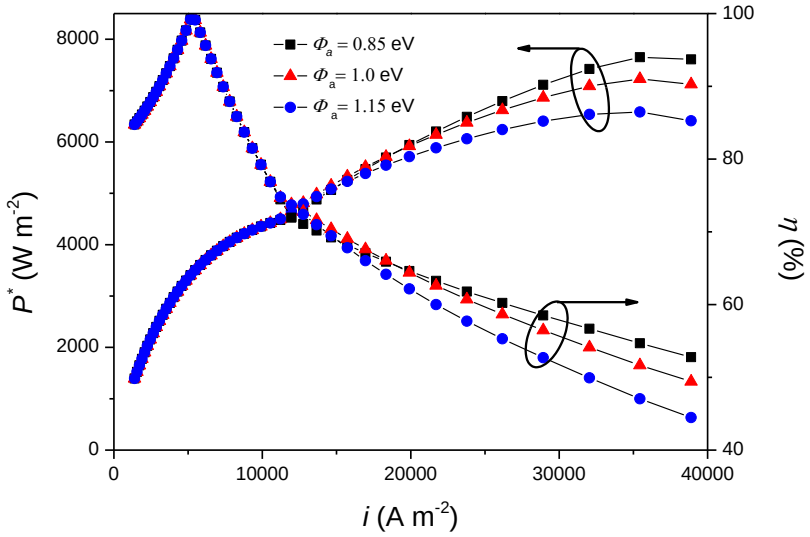

Fig. 11. Effects of the work function of VTIG anode on the system performance.